Synergistic marriage of CO_2 reduction and sulfide oxidation towards a sustainable co-electrolysis process

Kaixin Yang [a,1], Nan Zhang [b,1], Jiangfan Yang [a], Zhuo Xu [a], Junqing Yan [a], Deng Li [a,*], Shengzhong (Frank) Liu [a,c,**]

[a] Key Laboratory of Applied Surface and Colloid Chemistry, Shaanxi Engineering Lab for Advanced Energy Technology, School of Materials Science and Engineering, Shaanxi Normal University, Xi'an 710119, China
[b] School of Materials Science and Engineering, Shaanxi Normal University, Xi'an 710119, China
[c] Dalian National Laboratory for Clean Energy, Dalian Institute of Chemical Physics, Chinese Academy of Sciences, Dalian 116023, China

ARTICLE INFO

ABSTRACT

Current CO_2 electrolyzers suffer from low economic feasibility due to the huge energy demand of water oxidation and the recovery of low-value oxygen. Herein, an energy-efficient co-valorization electrolysis is reported by coupling CO_2 reduction with sulfide oxidation, utilizing a dual doped cobalt hydroxide anode and an electrochemical-reduced Bi cathode in a flow-cell electrolyzer. Benefiting from the accelerated reaction kinetics, the assembled electrolyzer saves 40% of the energy request to drive the CO_2RR-SOR electrolysis as compared to the CO_2RR-OER counterpart at 100 mA/cm^2. The CO_2 gas and S^{2-} pollutant are recycled to value-added formate and sulfur solid with Faraday efficiencies higher than 90%, doubling the net revenue of CO_2 electrolysis. Furthermore, a solar-driven CO_2RR-SOR system using a commercial Si cell was constructed to yield a current density of more than 100 mA/cm^2 during 6 h operation with a solar-conversion efficiency of 5.8 $\pm$ 0.4%, demonstrating a sustainable co-electrolysis system.

1. Introduction

Powering the world with renewable energy has become a global consensus to fulfill the mission of carbon neutrality and sustainability [1,2]. CO_2 reduction reaction (CO_2RR) via electrolysis offers a promising way to consume and accommodate green electricity from intermittent renewables while producing commodity fuels and chemicals [3,4]. The key challenge for the commercialization of present-day CO_2 electrolysis lies in the huge electricity expense from the high theoretical energy request and the sluggish surface catalytic kinetics, especially the oxygen evolution reaction (OER, $4OH^- \rightarrow O_2 + 2H_2O + 4e^-$) at the anode (Scheme 1a) [5,6]. Based on the thermodynamics, the anode water oxidation consumes up to 90% of the input energy, while only releasing low-value oxygen at the anode output [7,8]. Hence, CO_2 electrolysis of CO_2RR-OER couple actually "wastes" most of the input electricity, bringing down sustainability.

Minimizing the energy consumption while maximizing the economic benefits of CO_2 electrolysis by replacing the OER with alternatives has become an emerging strategy to tackle the "energy-waste" issue in the CO_2RR-OER electrolysis [9–14]. Sulfur production via sulfide oxidation reaction (SOR in alkaline with a pH near 14, $HS^- + OH^- \rightarrow S + H_2O + 2e^-$) offers an attractive candidate to be paired with CO_2RR (Scheme 1b), where the equilibrium potential to trigger the SOR is only 0.142 V vs reversible hydrogen electrode (RHE), comparing to the 1.229 V vs RHE for OER [15]. The CO_2RR-SOR couple then should potentially save the energy demand by at least 78% with respect to the CO_2RR-OER one (Scheme 1c, Table S1). On the other hand, as the second chalcogen element after oxygen, the sulfur product (0.22 $/kg) has a much higher market price than oxygen (0.085 $/kg), which could also increase the economic revenue at the anode in the CO_2RR-SOR process [16]. The anode revenue per unit energy input of the CO_2RR-SOR electrolyzer is estimated to be more than 20 times that of CO_2RR-OER one (Scheme 1c). Besides, the sulfide resources, such as H_2S from the raw natural-gas extraction fields or S^{2-} from the industrial sewage, are commonly

---

regarded as toxic pollutants against the eco-environment [17]. Then, the oxidation substances for SOR are negative-value waste chemicals and the waste-treatment characteristic of sulfide oxidation would further increase the value proposition of the CO_2RR-SOR process. Therefore, coupling CO_2RR with SOR may establish a sustainable co-electrolysis process for simultaneous CO_2 utilization and waste treatment.

To make the CO_2RR-SOR process economically feasible, the electrolyzer has to be operated at practical reaction rates (≥ 100 mA/cm^2) [18,19]. Though several groups have reported the synchronous CO_2 reduction and sulfur recovery via electrolysis, where the oxidation of sulfide to sulfur proceeded indirectly via the redox-couple cycles, such as EDTA-Fe^{3+}/EDTA-Fe^{2+}, I^{3-}/I$^-$ [20–22]. The theoretical oxidation potentials of these redox couples at the anode are inevitably higher than that of SOR, indicating that the cycle of the redox needs to consume extra energy with respect to the direct oxidation of sulfides. Moreover, as the oxidation of the sulfide by the redox proceeds as a chemical reaction process in the electrolyte, the mass transfer limitation of such indirect SOR in these reports would be more serious than the direct SOR electrolysis. Hence, the reaction rates of these electrolyzers are below 100 mA/cm^2 and the energy efficiencies are limited. To realize the benefits of co-electrolysis, the CO_2RR-SOR electrolyzer that has active and stable catalysts to rapidly reduce CO_2 and directly oxidize sulfide substrates is thus expected, which, however, has been rarely explored.

Herein, we report the coupling of CO_2RR with SOR for an energy-saving co-valorization process, yielding value-added CO_2-reduction chemicals and sulfur solids. Dual-doped cobalt hydroxides and gas-diffusion electrodes with electrochemical-reduced Bi catalysts are developed to catalyze the sulfide oxidation and the CO_2 reduction, respectively. A hybrid electrolyzer that utilizes the two electrodes is then applied for the long-term CO_2RR-SOR co-electrolysis at an industrial-level current density. A notable reduction of 40% in the energy demand is observed for the CO_2RR-SOR process with respect to the CO_2RR-OER one. Such a hybrid electrolyzer is further powered by a commercial Si solar cell to construct a photovoltaic-electrochemical (PV-EC) system for self-powered CO_2 reduction and sulfur recovery. An operation current density of more than 100 mA/cm^2 with a solar energy-conversion efficiency of $5.8 \pm 0.4\%$ is achieved on our PV-EC device.

2. Experimental

2.1. Chemicals and materials

All the chemicals were of analytical grade and used as received. Metal nitrate salts including $Cu(NO_3)_2$, $Ni(NO_3)_2 \cdot 6H_2O$, $Co(NO_3)_2 \cdot 6H_2O$, $Fe(NO_3)_3 \cdot 9H_2O$, $Bi(NO_3)_3 \cdot 5H_2O$, and urea, cetyltrimethylammonium bromide (CTAB) were purchased from Innochem. KOH, K_2S, NaF, and concentrated hydrochloric acid, ethanol, and isopropanol were purchased from Sinopharm. Nickel foam (NF, thickness=0.1 cm), gas diffusion electrode substrate (YLS-30 T), Sustainion

XA-9 ionomer (~5 wt% in ethanol), cation exchange membrane (Nafion 117) and anion exchange membrane (Fumasep, FAA-3-PK-75) were purchased from Suzhou Sinero Company. CO_2 (99.999%) and argon (99.999%) gases were supplied by Tenglong Gas Company. Ultrapure water (18.2 MΩ) was used in all experiments.

### 2.2. Preparation of dual-doped cobalt hydroxides for SOR

A hydrothermal method was adopted to prepare metal hydroxides on the NF [23]. Before the experiment, the NF (2×1.5 cm^2) plates were sequentially sonicated in 3 M HCl solution, ethanol, and ultrapure water for 15 min, followed by blow-dry using an air gun. Typically, 0.4 mmol metal nitrate ($Co(NO_3)_2$), 0.3 g urea, and 14 mL ultrapure water were mixed to form a clear solution. Then, the solution was transferred into a 50 mL Teflon-lined stainless-steel autoclave with a piece of NF being vertically immersed in the solution. The autoclave was put into the oven (Tianjin Taiste Instrument) and heated at 120 °C for 6 h. After cooling to room temperature, the NF grown with metal hydroxides was cleaned by ultrapure water and then immersed in the 1 M K_2S solution for 30 min for partial sulfurization. The final electrode was then washed and dried for further testing and characterization. The as-prepared electrode was sulfur-doped and denoted as S-Co@NF.

The procedure to prepare the transition metal-doped electrodes (denoted as S-M:Co@NF) was similar to that of S-Co@NF, except that the metal nitrate salts were changed during the hydrothermal process. The Cu-Co, Ni-Co, and Fe-Co mixed nitrate sources were adopted for the preparation of S-Cu:Co@NF, S-Ni:Co@NF, and S-Fe:Co@NF, respectively. The doping ratios of transition metal ions were controlled by tuning the feed ratios of metal nitrates during hydrothermal process.

2.3. Preparation of electro-reduced Bi and Cu GDE for CO_2RR

The ER-Bi (electro-reduced Bi) GDE was prepared according to the reported literature [24]. Basically, $Bi(NO_3)_3 \cdot 5H_2O$ (0.970 g) and CTAB (0.5 g) were added to 60 mL deionized water to form solution A. Taking another beaker, 3.0 g urea was dissolved into 40 mL ethanol to get solution B. Then, solution B was quickly added to solution A to form a white uniform mixture. After stirring in a water bath of 90 °C for 4 h, the suspension was centrifuged and the obtained powder was washed and then dried for use. To obtain the ER-Bi GDE, 10 mg of as-prepared Bi precursor powder, 2 mL of ethanol, and 40 μL of Nafion binder were mixed and then ultrasonicated for 2 h to obtain a homogeneous ink. Then, 180 μL ink was evenly dripped onto the YLS-30 T GDL substrate (1.5 cm × 1.5 cm). After drying at room temperature overnight, the GDE was pre-reduced at 100 mA/cm^2 in-situ to get the ER-Bi GDE. The bismuth metal mass loading of the ER-Bi GDE was controlled at 0.4 ± 0.05 mg/cm^2.

The ER-Cu GDE was likely prepared from the Cu(OH)F precursor. The Cu(OH)F powder was prepared by simply adding 3 mL 1 M $Cu(NO_3)$
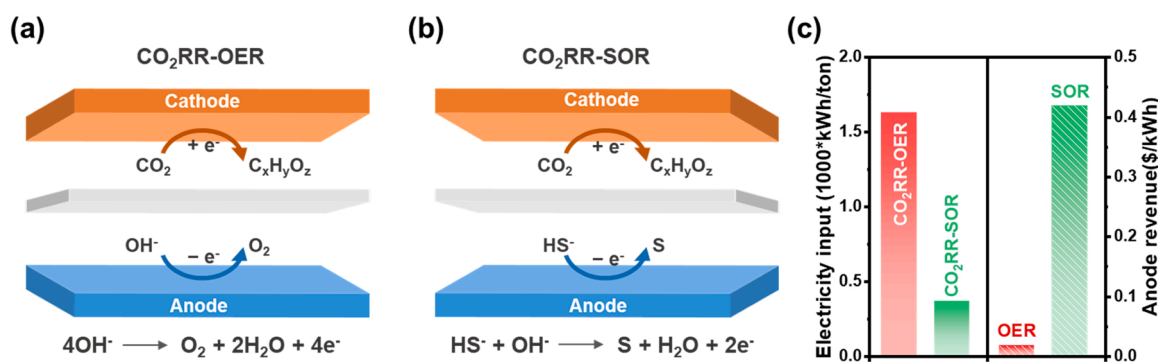
Scheme 1. Schematic of (a) CO_2RR+OER and (b) CO_2RR+SOR co-electrolysis systems. (c) Comparison of the electricity input (left) and the anode output revenue (right) of the two paired electrolysis systems. The calculation is based on the production of HCOOH.

solution into 10 mL 1 M NaF drop by drop. After stirring for 30 min, the suspended sediment was collected by centrifugation and then dried in a vacuum at 60 ℃ overnight. The procedure for the ER-Cu GDE preparation was similar to that of ER-Bi GDE, except the Cu(OH)F precursor was used.

2.4. Material characterization

X-ray diffraction (XRD) patterns of the samples were recorded on a Rigaku Smartlab-9 kW instrument using Cu Kα X-ray radiation at a scan rate of 2°/min. The morphologies of the catalysts were acquired using scanning electron microscopy (SEM, Hitachi Su8020) equipped with an energy-dispersive X-ray spectrometer (EDS, Horiba EX-270). Transmission electron microscopy (TEM) and high-resolution TEM (HRTEM) images were obtained on a JOEL JEM-2800 microscopy with an accelerating voltage of 200 kV. X-ray photoelectron spectroscopy (XPS) and Auger electron spectroscopy (AES) were conducted on a Thermo Scientific ESCALAB Xi spectrometer with an Al Kα X-ray source. C 1 s spectrum with peak intensity at 284.8 eV was used to calibrate all the binding energies. The UV–vis spectra of the anolyte were recorded on a Perkin-Elmer Lambda 950 spectrophotometer with a scan rate of 10 nm/min. An inductively coupled plasma optical emission spectrometer (ICP-OES) was conducted on Agilent 5110 to quantify the electrochemical dissolution of the electrodes.

2.5. SOR measurement in the H-type batch cell

The half-cell SOR measurement was conducted in an H-type batch cell. The S-Cu:Co@NF and other prepared anode were cut into a 2×1 cm^2 plate and were tested for SOR. The area of the anode immersed in the anolyte was controlled as 1 cm^2, where the upper part of the anode was covered by the electrically-insulated epoxy cover. Hg/HgO and platinum plate were used as the reference and counter electrodes, respectively. 1 M KOH and 1 M KOH+ 1 M K$_2$S were used as the catholyte and anolyte, respectively. A Nafion 117 membrane was used to separate the anolyte and catholyte. During the test, the anolyte and catholyte were continuously stirred. The LSV tests were performed at a scan rate of 5 mV/s, aiming to evaluate the SOR activity of the anodes. Potentiostatic electrochemical impedance spectroscopy (EIS) was conducted at 0.5 V vs RHE. The stability test was conducted as chronopotentiometry at 100 mA/cm^2, where the anolyte was sampled and refreshed every 4 h. UV–vis spectrometry was adopted to detect the oxidation product of S^{2-}.

2.6. CO$_2$RR measurement in the flow cell

CO$_2$ electroreduction experiments were performed in a three-electrode flow cell with serpentine flow fields. The ER-Bi GDE, an Ag/AgCl electrode, and a nickel foam were used as the working, reference, and counter electrodes, respectively. The CO$_2$ gas was fed at a constant flow rate of 20 mL/min using a mass flow controller (Beijing Sevenstar, CS200D). 1.0 M KOH aqueous solution (40 mL) was used as both the catholyte and anolyte and a cation exchange membrane (Fumasep, FAA-3-PK-75) was used to separate the anolyte and catholyte. The electrolytes were circulated through the anode and cathode chamber individually at a flow rate of 10 mL/min using two peristaltic pumps. The thickness of the cathode chamber was 10 mm. The CO$_2$RR measurements were conducted using the galvanostatic method with gradually increasing the applied current densities. Potentiostatic electrochemical impedance spectroscopy (EIS) was conducted at open circuit potential after the galvanostatic measurements to determine the solution resistance (R_s). The potentials at the working electrode versus the reversible hydrogen electrode (RHE) were corrected based on the R_s.

The gas products were analyzed online using a gas chromatograph (GC, Agilent GC7890B) which was equipped with a thermal conductivity detector (TCD) and a flame ionization detector (FID) for H$_2$, CO, and CH$_4$, C$_2$H$_4$ quantification, respectively. A Porapak-Q column to pre-separate all the gases, a Molecular sieve-5A column to separate H$_2$, CO, and a Porapak-N column to separate CH$_4$, C$_2$H$_4$, and CO$_2$ were used. Argon gas was used as the carrier for the gas chromatograph. The liquid products were collected from the catholyte and quantified by ^{1}H nuclear magnetic resonance spectroscopy (NMR, JEOL JNM-ECZ400R/S1). The sampling time of both gaseous and liquid products was 10 min after each electrochemical measurement started, and three individual tests were conducted to acquire the final data with error bars.

2.7. Two-electrode CO$_2$RR-SOR measurement

The same flow cell that was used for half-cell CO$_2$RR was adopted for the two-electrode CO$_2$RR-SOR measurement. The ER-Bi GDE and S-Cu:Co@NF were used as the cathode and anode, respectively. 1 M KOH (40 mL) and 1 M KOH+ 1 M K$_2$S (40 mL) were used as the catholyte and anolyte, respectively. A Nafion 117 membrane was used. The other test conditions were similar to the half-cell CO$_2$RR test. The gaseous and liquid CO$_2$RR products were analyzed by GC and NMR respectively, while the anodic oxidation product of S^{2-} was monitored by UV–vis spectrometry.

For the solar-driven CO$_2$RR-SOR measurement, a commercial Si PV cell (5×5 cm^2, 0.38 W) under irradiation was used as the power source to drive the two-electrode CO$_2$RR-SOR co-electrolysis process. The simulated sunlight was provided by the high uniformity integrated Xenon light source equipped with an AM 1.5 G filter (Beijing Perfectlight, PLS-FX300HU), where the light intensity at the surface of the PV cell was calibrated as 100 mW/cm^2. The volumes of anolyte and catholyte were scaled up to 200 mL. The flow rates of CO$_2$ gas, the catholyte, and the anolyte were kept unchanged. The Keithley 2450 source meter was used to measure and record the current in the circuit during the solar-driven CO$_2$RR-SOR co-electrolysis process. The voltage in the circuit was measured per hour using a multimeter. The outlet gas, catholyte, and anolyte were sampled every hour.

2.8. Voltage breakdown analysis of the CO$_2$RR-SOR cell

The potential difference between the anolyte (1 M KOH + 1 M K$_2$S) and catholyte (1 M KOH) was determined by measuring the open-circuit potential between two reference electrodes which were immersed in the anolyte and catholyte separately. The anode overpotential for SOR (η_a) and cathode overpotential for CO$_2$RR (η_c) were determined from the half-cell SOR and CO$_2$RR tests. The voltage loss in the membrane (E_m) was calculated based on the differences between the cell resistances of the two-electrode cell with or without a Nafion membrane. 3 M KOH was used as the electrolyte, mimicking the cation charge transport of the electrolyte containing 1 M K$_2$S and 1 M KOH. The voltage losses caused by the solution resistances (E_s) were calculated by subtracting E_m from the full cell ohmic loss of the two-electrode CO$_2$RR-SOR cell operating at 100 mA/cm^2.

2.9. DFT calculation

Density Functional Theory (DFT) calculations were performed using the Vienna Ab-initio Simulation Package software [25,26]. The generalized-gradient approximation by Perdew, Burke, and Ernzerhof was employed for the exchange-correlation energy [27]. The projector-augmented wave pseudopotentials are used in the calculations. The van der Waals interaction has been considered using the Grimme scheme [28]. All structural optimizations were performed by using a cut-off at 450 eV for the plane-wave basis set. A (4×4) supercell of a (001) facet of Co(OH)$_2$ was built to module the surface. The supercells have four atomic layers and a vacuum spacing of 15 Å along the surface's normal direction to avoid interactions between images. The convergence of energy and forces were set to 1×10^{-5} eV and 0.02 eV/Å, respectively. The free energies of the intermediates were obtained by ΔG

$= \Delta E + \Delta ZPE - T\Delta S$, where ΔE, ΔZPE, ΔS are the differences of DFT total energy, zero-point energy, entropy change, respectively. The T is the temperature.

3. Results and discussion

3.1. Designing SOR catalysts: dual-doped cobalt hydroxide

The cobalt-based hydroxides are designed to catalyze the anodic SOR, considering their superior OER activity and good stability. Specifically, Cu, Ni, and Fe heteroatoms were introduced to the cobalt hydroxide to tune the electronic structures and hence activities. Besides, as the sulfion ions would potentially implant into the hydroxide structure during the SOR process due to the significant difference in solubilities between the sulfide and hydroxide, the sulfurization of the hydroxides to dope S atoms was further conducted to pre-activate the catalysts [23]. Hence, a dual-doped cobalt hydroxide catalyst is designed for sulfide oxidation. The cobalt-based hydroxides were in-situ grown on the bare nickel foam (NF) via a hydrothermal process, and the as-prepared electrodes are inferred as M:Co@NF, where M represents the doping heterometals. The sulfurization of these electrodes was then performed by ion-exchange treatment in 1 M K_2S, and the corresponding electrodes are denoted as S-M:Co@NF. To make a simple and reasonable comparison of different dual-doped electrodes, the doping ratio of metal nitrate of Ni, Fe, and Cu, and the condition of sulfurization treatment during the synthesis were set as the same.

X-ray diffraction (XRD) patterns of the electrodes before and after sulfurization all showed only strong peaks of metallic Ni, which may be caused by the too-strong peaks of the NF and the low content of the grown catalysts on the NF substrate (Fig. S1). Raman spectra of the as-prepared Co@NF showed characteristic bands at 472, 520, and 668 nm corresponding to the Co-O vibrations of α-$Co(OH)_2$, and these bands would maintain after the metal doping (Fig. S2a) [29–31]. After sulfurization, the band at 472 nm survived and new bands at 446, 530, and 686 nm were observed, indicating the preservation of the $Co(OH)_2$ structure and the partial replacement of O atom by S dopants after sulfurization (Fig. S2b).

The morphology evolution of $Co(OH)_2$ after hetero metal and S doping was investigated via scanning electron microscopy (SEM). Typically, for the Cu, S co-doping case, SEM images of Co@NF, Cu:Co@NF, and S-Cu:Co@NF showed that the surface of bare NF was well covered by a catalyst layer (Fig. S3). Initially, the as-prepared Co@NF
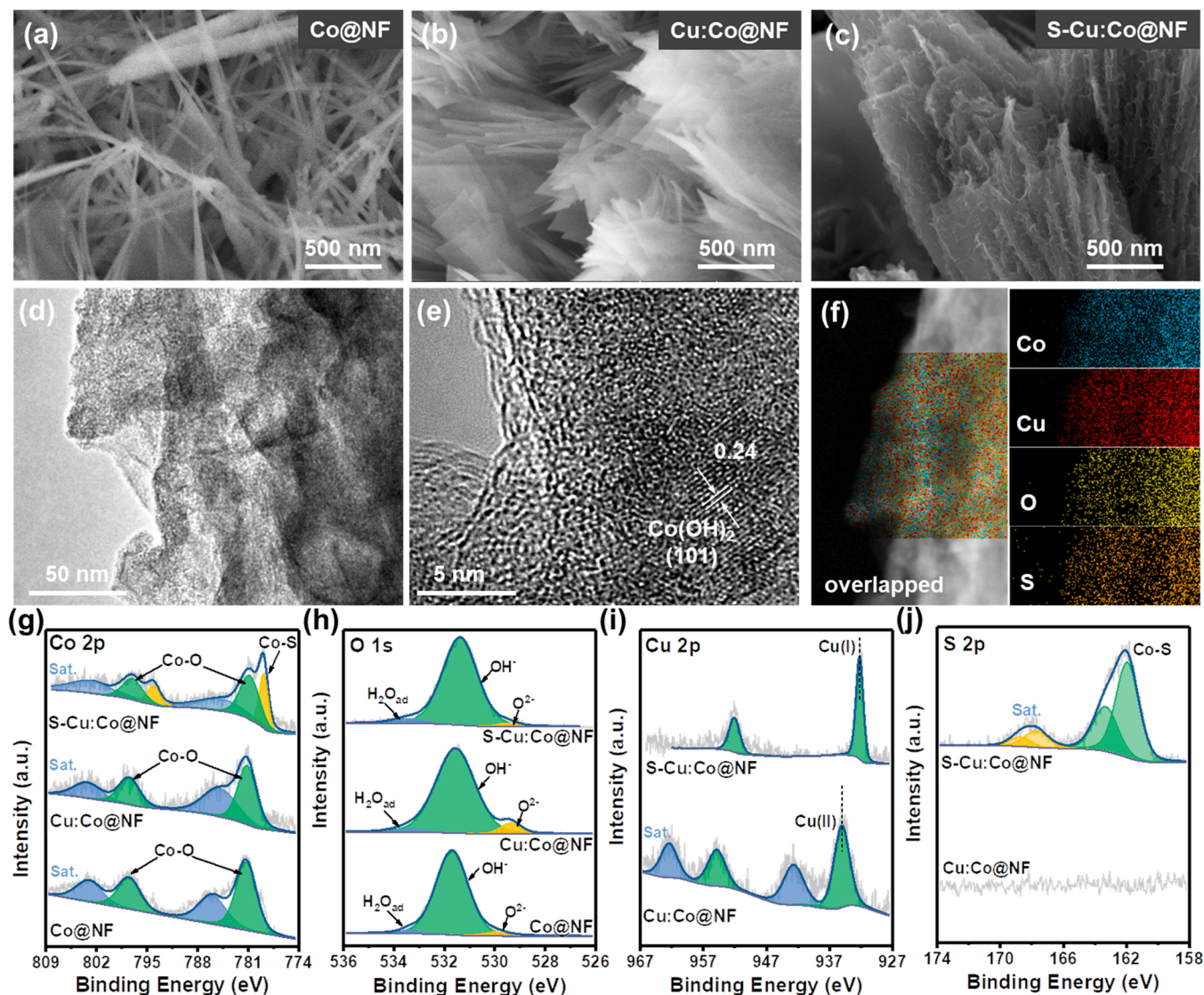
Fig. 1. SEM images of (a) Co@NF, (b) Cu:Co@NF, and (c) S-Cu:Co@NF catalyst. (d) and (e) HRTEM image of S-Cu:Co@NF. (f) Overlapped elemental mapping of S-Cu:Co@NF and the corresponding elemental mapping of Co, Cu, O, and S signals. (g) Co 2p and (h) O 1s XPS spectra of the Co@NF, Cu:Co@NF, and S-Cu:Co@NF. (i) Cu 2p and (j) S 2p spectra of Cu:Co@NF and S-Cu:Co@NF.

showed a morphology of nanoneedles, which is a typical structure of the $Co(OH)_2$ (Fig. 1a) [32]. The addition of Cu dopants would change the morphology of $Co(OH)_2$ to another typical structure of nanoplates (Fig. 1b), indicating that the Cu ions would tune the crystal-growth orientation of $Co(OH)_2$ during the hydrothermal process [33,34]. Further doping S atoms into the Cu:Co@NF, the morphology evolved to fluffy lamellas, suggesting a structure reconstruction during the S atom ion-exchange process (Fig. 1c). High-resolution transmission electron microscopy image of S-Cu:Co@NF also confirms the lattice fringe of 0.24 nm for S-Cu:Co@NF, which can be attributed to the (101) plane of $Co(OH)_2$ (Fig. 1d-e). It is also noted that there exists an amorphous surface layer of the S-Cu:Co@NF, which may be due to the doping of Cu or S atoms. The elemental mapping images further show that the signals of Co, Cu, O, and S elements are well overlapped with each other (Fig. 1f), suggesting that the Cu and S are uniformly doped in $Co(OH)_2$. It is concluded that $Co(OH)_2$ is successfully doped with Cu and S atoms. As a comparison, the Ni or Fe doped $Co(OH)_2$ showed micro-morphologies of nanoneedles similar to the pristine $Co(OH)_2$, except that the nano-needles are in clusters (Fig. S3). The sulfurization of Ni:Co@NF and Fe:Co@NF showed a small influence on the nano-needle morphology except the surface reconstruction (Fig. S4). The elemental mapping results of S-Ni:Co@NF and S-Fe:Co@NF also confirm the uniform doping of Ni, S or Fe, S atoms (Fig. S5). The atomic ratios of metal dopants and S for different electrodes were also semi-quantified and the metal-doping ratios of different electrodes were comparable, while the S doping ratio of S-Cu:Co@NF was higher than the others (Table S2).

XPS analysis was further conducted to investigate the valence-state change of $Co(OH)_2$ after Cu and S doping. For the intrinsic Co@NF, the Co 2p peaks at 797.7 and 781.0 eV are assigned to the Co $2p_{1/2}$ and Co $2p_{3/2}$ of Co-O bonds for $Co(OH)_2$ and the corresponding OH^- at 531.7 eV is also identified in O 1 s XPS spectra (Fig. 1g-h). The weak O 1 s peaks at 533.4 and 529.8 eV are assigned to absorbed water and oxide species, respectively [23]. After Cu doping, there was no obvious change in the binding energies of Co 2p and O 1 s, while the Cu 2p spectra showed characteristic peaks of Cu $2p_{1/2}$ (954.9 eV) and Cu $2p_{3/2}$ (935.1 eV), corresponding to the Cu(II) species (Fig. 1i) [35]. After sulfurization, the Co 2p spectrum of S-Cu:Co@NF showed an extra doublet at 794.1 and 778.9 eV, which could be assigned to the new-formed Co-S bonds (Fig. 1g). The Co-S bonds were further evidenced by the S 2p peaks at 163.3 eV (S $2p_{1/2}$) and 161.9 eV (S $2p_{3/2}$) (Fig. 1j). In addition, as the redox potential of Cu(II)/Cu(I) (0.86 V vs RHE) is much higher than that of S/S^{2-} (0.142 V vs RHE), the reduction of Cu(II) dopants to Cu(I) species during sulfurization is expected. Indeed, the Cu 2p peaks of S-Cu:Co@NF were negatively moved to 952.2 and 932.3 eV, which can be assigned to the Cu(I) species (Fig. 1i). The Cu LMM Auger electron spectra (AES) further supported the formation of Cu(I) species from the reduction of Cu(II) dopants during the S-doping process (Fig. S6) [36].

The SOR activities of these electrodes were evaluated in an H-type batch cell. The anolyte was chosen as 1 M KOH containing 1 M K_2S, considering that aqueous KOH solutions are more popular in the CO_2RR field. In such anolyte (pH = 13.6), the main sulfuric species existing in the solution are HS^- ions and the SOR proceeds as the oxidation of HS^- species [37]. Also, due to the rapid dissolution of sulfur in the alkaline electrolyte, the oxidation of sulfide would produce soluble polysulfides instead of sulfur solids [37]. As the sulfur doping of hydroxides in the sulfide solution is a spontaneous process, the immersion of Co@NF in the anolyte would keep doping the S atoms into the Co@NF electrode. With the repeat of the linear sweep voltammetry (LSV) test, it is observed that the SOR activity of the Co@NF electrode kept increasing with the repeat times (Fig. S7a), demonstrating that the S doping would easily promote the SOR activity of the hydroxides. Meanwhile, for the pre-activated $Co(OH)_2$ after 30 min S-doping treatment, the SOR activity reached a stable performance as shown in Fig. S7b. We further optimized the feeding ratios of Cu/Co metal nitrates for the hydrothermal process and the feeding ratio of 1:4 for Cu/Co was adopted for

the preparation of the champion S-Cu:Co@NF electrode (Fig. S7c-d).

Fig. 2a displays the LSV curves of the S-Co@NF and other dual-doped S-M:Co@NF electrodes. It is found that the S-Cu:Co@NF showed the best performance for SOR among all the tested electrodes. Specially, at 0.5 V vs RHE, the acquired current densities for different electrodes are 175.3, 102.2, 66.6, and 40.1 mA/cm^2 for S-Cu:Co@NF, S-Co@NF, S-Ni:Co@NF and S-Fe:Co@NF, respectively. To give a precise comparison of the intrinsic SOR activity of the dual-doped catalysts, the electrochemical active surface areas (ECSA) of the electrodes were also estimated (Fig. S8, Table S3) and the ECSA-normalized current densities (J_{ECSA}) at 0.5 V were compared. The activities of the electrodes based on J_{ECSA} are still in the same order as above, where the J_{ECSA} of S-Cu:Co@NF was 2.6, 3.3, and 3.4 times that of S-Co@NF, S-Ni:Co@NF, and S-Fe:Co@NF, respectively (Fig. 2b). It is indicated that the Cu, S-dual doping would profoundly improve the activity of $Co(OH)_2$, while the Ni, S- or Fe, S-dual doping would not. To gain further insight into the surface reaction kinetics, we revisited the LSV curves to conduct the Tafel slope analysis (Fig. S9). The Tafel slopes of S-Cu:Co@NF, S-Co@NF, S-Ni:Co@NF, and S-Fe:Co@NF were determined as 89, 128, 147, 224 mV/dec, respectively, where the S-Cu:Co@NF exhibited the lowest value of Tafel slope. The potentiostatic electrochemical impedance spectrometry (EIS) was further conducted to investigate the catalytic charge transfer kinetics at the electrode/electrolyte interface (Fig. 2c). The charge transfer resistance (R_{ct}) is estimated by the diameter of the semicircle of the Nyquist plot. It is found that the S-Cu:Co@NF had the smallest semicircle and hence the lowest R_{ct} as compared to the others, signifying the superior SOR activity of the S-Cu:Co@NF electrocatalyst.

To unravel the effect of metal dopants on tuning the electronic structure and hence the SOR activity of S-$Co(OH)_2$, density-functional theory (DFT) calculations of the band structures of S-M:Co@NF were carried out [38]. The density-of-state profile of S-Co@NF shows that there exist inter-band states above the Fermi level of $Co(OH)_2$, which could be attributed to the S doping (Figs. 2d and S10). While, for the S-Cu:Co@NF, the Cu dopants would lead to the formation of more unoccupied states above the Fermi level of S-$Co(OH)_2$, while the Ni or Fe dopants would eliminate all these states (Fig. 2d). Hence, the continuous band around E_f for S-Cu:Co@NF would contribute to the high electric conductivity and the facilitated electron transfer as compared to the S-Co@NF, S-Ni:Co@NF or S-Fe:Co@NF electrodes, resulting in the superior SOR activity of S-Cu:Co@NF [38,39]. The reaction kinetics of SOR on different electrodes was further investigated via the DFT calculation, where the adsorption free energies of the key intermediate of S* on different electrodes were obtained [40]. The structural models of S* adsorption on different electrodes are displayed in Fig. 2e, demonstrating that the metal dopants would contribute to the adsorption of the S* intermediate. Basically, the oxidation of HS^- species is proceeded in the following steps: a. initial HS^- adsorption, b. formation of an intermediate S* state via electroreduction, c. desorption of S* to produce S, d. dissolution of S in the alkaline electrolyte to form S_x^{2-} [37, 41]. Too weak or too strong binding strength of the S* intermediate on the electrode surface is of no advantage to the SOR catalysis [40,42]. Therefore, a good SOR catalyst should exhibit an appropriate free energy that approaches zero for S* adsorption ($|\Delta G_{S*}| \approx 0$ eV) [40]. As shown in Fig. 2f, the $|\Delta G_{S*}|$ of S-Cu:Co@NF is only 0.17 eV, which value is closest to zero as compared to those of other electrodes. This is in good agreement with the better SOR activity of S-Cu:Co@NF with respect to others. While, the S-Ni:Co@NF (0.24 eV) and S-Fe:Co@NF (0.28 eV) show larger values of $|\Delta G_{S*}|$ as compared to the pristine S-Co@NF (0.20 eV), confirming the worse SOR activities of the former two electrodes. It is then concluded that the Cu dopants would tune the electronic structure of S-$Co(OH)_2$ by forming inter-band states and adjusting the adsorption of S* intermediate to a suitable strength, hence facilitating the catalytic kinetics and promoting the SOR activity of S-$Co(OH)_2$.
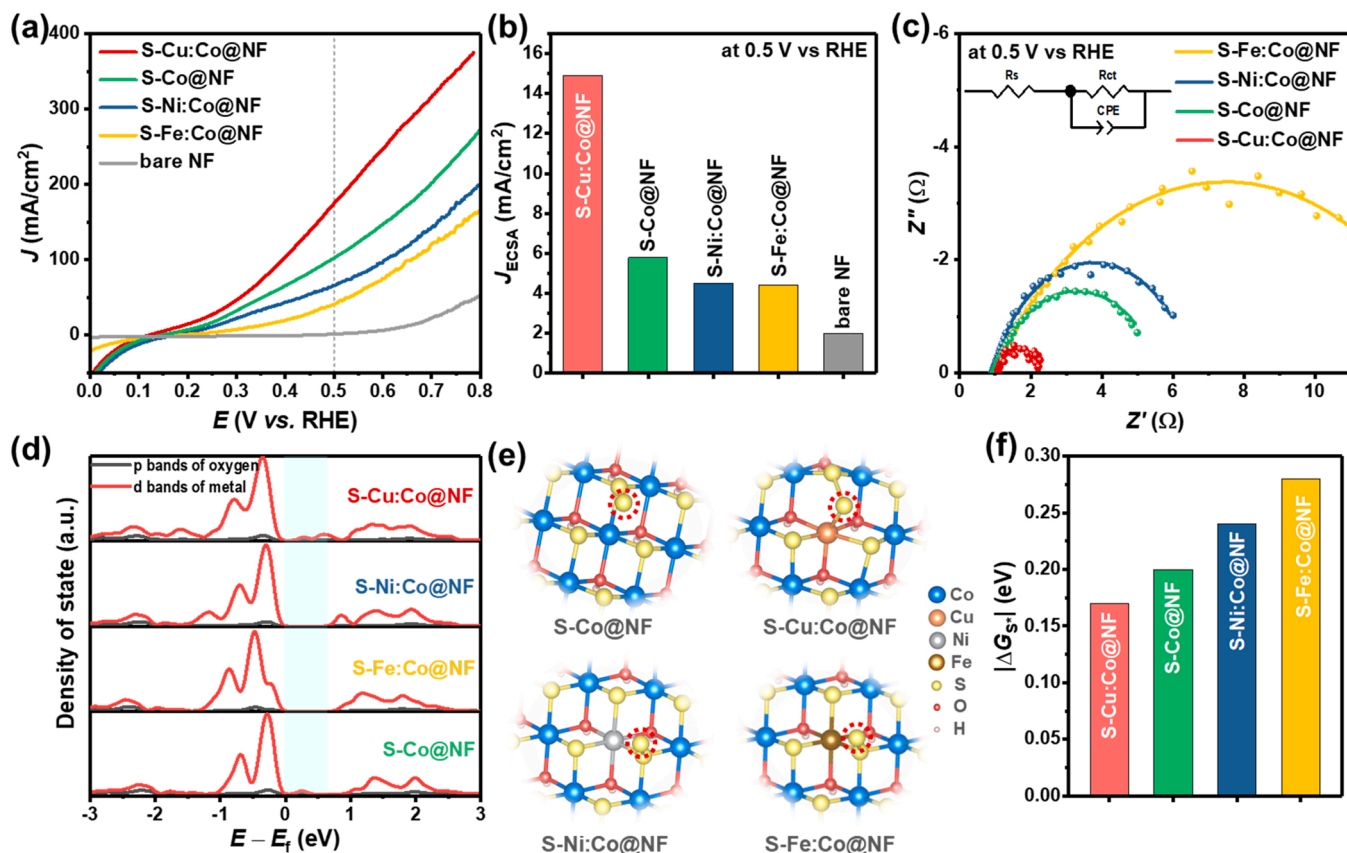
Fig. 2. (a) LSV curves of S-Co@NF, S-Cu:Co@NF, S-Fe:Co@NF, S-Ni:Co@NF, and bare NF electrodes. (b) Comparison of ESCA-normalized current densities (J_{ECSA}) of different electrodes at 0.5 V vs RHE. (c) Potentiostatic EIS results and fitted curves for different electrodes tested at 0.5 V_{RHE}. Inset shows the equivalent circuit. (d) The calculated density of states (DOS) of and (e) structural models of S* intermediate adsorption on different electrodes. (f) Gibbs free energies for the formation of adsorbed S* intermediates on different electrodes.

3.2. SOR performance at the anode

The optimal S-Cu:Co@NF electrode was then adopted as the anode catalyst to construct the CO_2RR-SOR coupling electrolyzer. The SOR and OER activity of the S-Cu:Co@NF was firstly compared (Fig. 3a). The LSV curves indicate that the S-Cu:Co@NF required 0.381 V vs RHE to achieve a current density of 100 mA/cm^2, corresponding to an overpotential of 239 mV. In contrast, the energy demand for sluggish OER on S-Cu:Co@NF at identical current density was 1.672 V vs RHE, which is more than 4 times that for SOR. The appreciable reduction of the operation potential suggests that more than 77% of the electricity input is saved for the anodic oxidation reaction. The yielding of anodic product in SOR was further detected by monitoring the UV–vis spectra of the anolyte, given that polysulfides are the actual oxidation products in alkaline solutions [37]. As the polarization at 100 mA/cm^2 proceeded, a gradual rise of UV–vis absorption bands at 300 nm and 370 nm was observed, accompanied by the color of the anolyte turning from achromatous to orange (Fig. 3b and Inset in Fig. 3d). The absorption bands at 300 nm and 370 nm for the sampled anolytes were characteristics of short-chain polysulfides (S_x^{2-}, $2 \leq x \leq 4$) with S_2^{2-} as the main component [16,40]. As we plotted the total electricity quantity passed through the circuit against the absorption peak intensities at 300 nm, it is found that there existed a nonlinear relationship at the beginning of SOR polarization and then a linear relationship was built right after the 0.75 h-test (Fig. S11). It is indicated that during the SOR polarization test, the polysulfides experienced a possible adsorption by the electrodes and chambers at the beginning and then were produced at the anode with a reasonable Faradaic efficiency (FE) of 100%. After 4 h of polarization, the acquired anolyte full of S_2^{2-} could be treated with acid to

yield the yellow powder, which corresponds to the elemental sulfur solid (Figs. 3c and S12).

The SOR test at 100 mA/cm^2 was further extended to 16 h to evaluate the durability of the S-Cu:Co@NF electrode. As depicted in Fig. 3d, the potential at the anode varied in the range from 0.375 to 0.4 V vs RHE, which could be attributed to the intermittent refresh of the anolyte. When ignoring these fluctuations, the activity of the catalyst showed little decay during the 4-cycle test, demonstrating the good stability of the S-Cu:Co@NF for SOR. The charge transfer resistance of the anode for SOR was also investigated and the value of resistance showed small change along the durability test, demonstrating the stable catalytic ability of the S-Cu:Co@NF electrode (Fig. S13). SEM images of the electrode after the durability test suggested that the lamella structure of the catalyst was maintained (Fig. S14). Postmortem XPS and AES analysis showed that the Co 2p, Cu 2p, O 1 s, S 2 s, and Cu LMM spectra were similar to those of S-Cu:Co@NF before the test (Fig. S15), ruling out the formation of pure sulfides, oxyhydroxides or oxides. It is also noted that the peak intensities of Co-S species were increased with respect to that of Co-O bonds, which can be attributed to the in-situ surface sulfurization of the catalyst during the long-term test. This is similar to the phenomenon in OER catalysis, where the surface of catalysts tends to be oxidized during the test [43]. The anolyte after the durability test was also analyzed by the ICP-OES technique to quantify the possible released metal ions from the electrode, where the amounts were determined as 0.013, 0.021, and 0.033 mg/L for Cu, Co, and Ni, respectively. The rather low dissolution of the S-Cu:Co@NF during the polarization clearly indicates that the performance of the electrode for SOR is not from the sacrifice of the electrode itself. All the above results support that the S-Cu:Co@NF electrode is able to catalyze the SOR stably
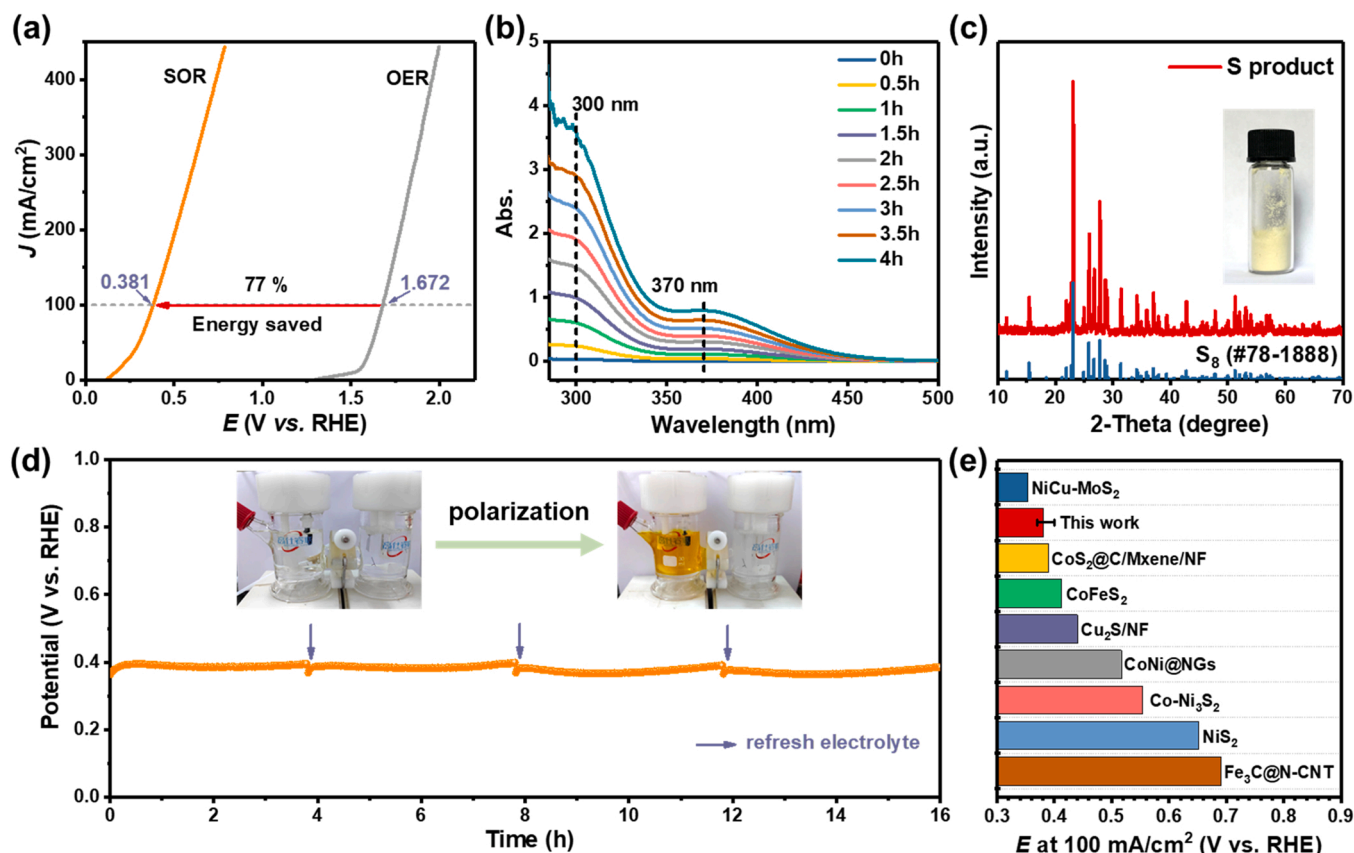
Fig. 3. (a) Polarization curves of SOR and OER on S-Cu:Co@NF electrodes. (b) UV–vis spectra of 50 times diluted anolyte sample during the 4-hours SOR polarization test at 100 mA/cm^2. (c) XRD pattern of the collected S powder. The inset is the digital photo of the S powder. (d) Durability of the S-Cu:Co@NF electrode for SOR polarization at 100 mA/cm^2. The arrows marked the refreshing of the anolyte. The inset photos showed the color change of the anolyte during the SOR polarization. (e) Comparison of energy requests at 100 mA/cm^2 for the S-Cu:Co@NF and reported electrodes for SOR.

with a high activity. To highlight the catalytic performance of the S-Cu:Co@NF for SOR, the potential request at 100 mA/cm^2 derived from the chronopotentiometry test was compared with those of recently reported SOR catalysts (Fig. 3e and Table S4) [16,40,44–49] It is demonstrated that our S-Cu:Co@NF is among the best for SOR.

3.3. Coupling SOR with CO$_2$RR for a sustainable electrolysis

At the cathode side, the CO$_2$RR catalysts that have low onsets and fast responses to the increase of applied potentials are preferred. Inspired by the fact that the electrochemical reduced Bi (ER-Bi) catalysts are efficient for CO$_2$RR, we chose the recently reported Bi-derived catalysts as the cathode [24]. The Bi precursor was prepared by a simple chemical precipitation method by hydrolyzing the Bi(NO$_3$)$_2$ in the urea solution under a water bath of 90 ℃. XRD pattern of the collected powder indicates the formation of Bi$_2$O$_3$ (JCPDS #29–0236) (Fig. S16a). The catalyst ink containing Bi$_2$O$_3$ and ionomers was then drip-coated on the gas diffusion layers (GDL) and then in-situ reduced in the CO$_2$RR test cell to get the ER-Bi gas diffusion electrode (GDE). XRD patterns of the GDE before and after electrochemical reducing treatment suggest that the Bi$_2$O$_3$ was reduced to metallic Bi (JCPDS #44–1246) (Fig. S16a). SEM image of the ER-Bi GDE shows that bismuth nanoplates with good homogeneity were formed (Fig. S16b-c). High-resolution transmission electron microscopy (HRTEM) image suggests the lattice spacing of 0.322 nm of reduced catalysts, corresponding to the Bi (012) plane (Fig. S16d-e). The Bi 2p XPS spectra further confirm the existence of Bi^0 metal for the ER-Bi GDE (Fig. S16f).

The CO$_2$RR performance of the obtained ER-Bi GDE was then evaluated in a three-electrode flow cell. The ER-Bi GDE exhibited a low onset

potential of − 0.430 V vs RHE (reaching 5 mA/cm^2) and required only − 0.648 V vs RHE to launch a current density of 100 mA/cm^2 (Fig. 4a). The durability of ER-Bi GDE was also examined by prolonged polarization test at 100 mA/cm^2. During the 8 h test, the ER-Bi GDE cathode could stably operate at around − 0.65 V vs RHE to continuously produce HCOO$^-$ with a FE higher than 90% (Fig. S16g).

A two-electrode electrolyzer that utilizes ER-Bi GDE cathode and S-Cu:Co@NF anode (ER-Bi GDE||S-Cu:Co@NF) was then constructed for a co-valorization electrolysis. Based on the electrochemical performance of ER-Bi GDE for CO$_2$RR and S-Cu:Co@NF for SOR and OER, the chemistry of coupling CO$_2$RR and SOR could cut the cell voltage down by one fold relative to the common CO$_2$RR-OER electrolysis (Fig. 4a). The two-electrode CO$_2$RR-SOR electrolysis was then conducted in an asymmetric configuration using 1 M KOH as the catholyte and 1 M KOH with 1 M K$_2$S as the anolyte, where a cation exchange membrane (CEM) was used to ensure the K$^+$ transport and restrict the HS$^-$ crossover. The potential difference between the anolyte and catholyte was measured as + 26 mV. For the CO$_2$RR-OER electrolysis that used 1 M KOH as both the anolyte and catholyte, an anion exchange membrane (AEM) was preferred. Fig. 4b displays the polarization curves of the CO$_2$RR-SOR and CO$_2$RR-OER electrolysis in the two-electrode ER-Bi GDE||S-Cu:Co@NF electrolyzer. The CO$_2$RR-SOR electrolysis showed a low onset cell potential of 0.75 V and delivered a current density of 100 mA/cm^2 at a low full cell voltage of 2.10 V, cutting 40% of the electricity demand relative to the CO$_2$RR-OER system. The polarization curves at 100 mA/cm^2 of the CO$_2$RR-SOR and CO$_2$RR-OER electrolysis further evidenced the decreased energy demand of the former one (Fig. S17). Furthermore, an electrolyzer that utilizes Pt as the anode for OER (ER-Bi GDE||Pt) was also built to conduct the CO$_2$RR-OER co-electrolysis at 100 mA/cm^2,
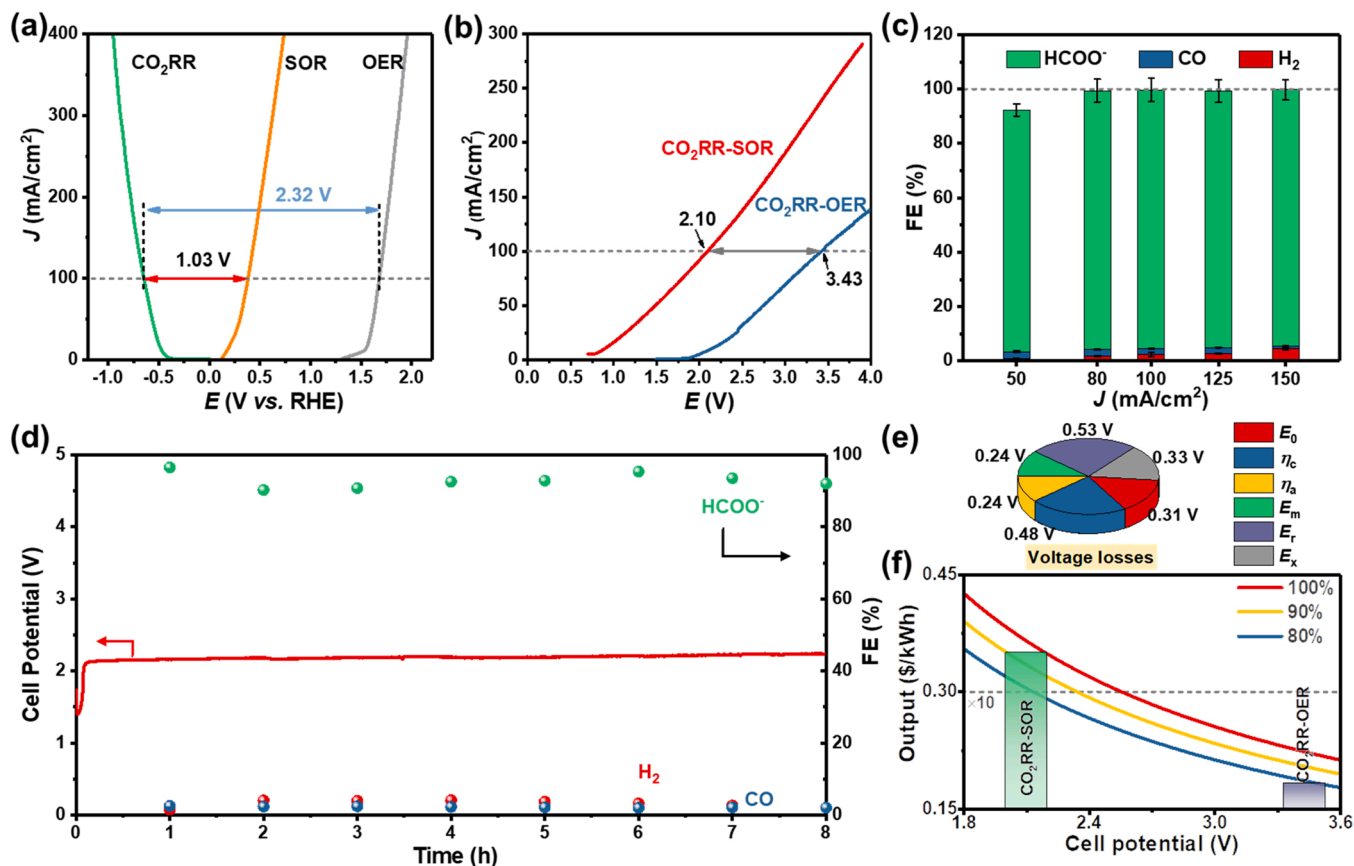
Fig. 4. (a) Overlay of voltage-current density curves of CO$_2$RR on ER-Bi GDE, SOR and OER on S-Cu:Co@NF. (b) Polarization curves of the two-electrode CO$_2$RR-SOR and CO$_2$RR-OER systems utilizing ER-Bi GDE cathode and S-Cu:Co@NF anode. (c) Faradaic efficiencies of reduction products at different current densities for the two-electrode CO$_2$RR-SOR system. (d) Durability test of the two-electrode CO$_2$RR-SOR system using S-Cu:Co@NF||ER-Bi GDE cell at 100 mA/cm^2. (e) Voltage breakdown analysis of the two-electrode CO$_2$RR-SOR electrolyzer. (f) Techno-economic analysis of the two-electrode CO$_2$RR-SOR and CO$_2$RR-OER systems, where the output revenue per unit electricity input varies with the cell potential and the FE of HCOO$^-$. The estimated cost line corresponding to 10 times the electricity price was also drawn.

where the cell voltage is still much higher than that for CO$_2$RR-SOR using the ER-Bi GDE||S-Cu:Co@NF cell. As such, we demonstrated the advantage of CO$_2$RR-SOR coupling for an energy-saving co-electrolysis process.

The product outputs at the cathode and anode of the two-electrode CO$_2$RR-SOR electrolyzer were further studied (Fig. S18). Fig. 4c shows the FEs of different reduction products as a function of applied current densities. H$_2$, CO, and HCOO$^-$ were produced at the cathode with HCOO$^-$ as the main product. During the range from 50 to 150 mA/cm^2, the FE of HCOO$^-$ was kept at more than 90% with a value of 95.1% at 100 mA/cm^2. The anode products at different current densities were also detected via UV–vis spectrometry. It is found that the accumulated concentration of S$_2^{2-}$ increased linearly with the applied current density (Fig. S19), indicating that no oxygen evolution was involved in the two-electrode CO$_2$RR-SOR electrolysis. The ER-Bi GDE||S-Cu:Co@NF electrolyzer also demonstrated high durability to perform the CO$_2$RR-SOR electrolysis at 100 mA/cm^2 for over 8 h, where the applied cell voltage maintained at around 2.1 V (Fig. 4d). This low full-cell voltage of our CO$_2$RR-SOR couple is also among the best performance of most other CO$_2$RR-paired electrolysis systems (Table S5), such as CO$_2$RR-methanol oxidation, CO$_2$RR-glycerol oxidation, etc [7,23,50–53].

The voltage breakdown analysis of the CO$_2$RR-SOR cell was further conducted, aiming to guide the future optimization of the system (Fig. 4e). Basically, the CO$_2$RR-SOR couple has different thermodynamic energy requests (E^0) depending on the reduced products at the cathode side. For CO$_2$RR-SOR to produce HCOO$^-$, the E^0 of the CO$_2$RR-SOR is only 0.31 V, which is ~1.79 V lower than the operation voltage

(~2.1 V) of CO$_2$RR-SOR at 100 mA/cm^2, indicating that most of the input energy is consumed by the catalytic overpotentials and cell resistances. The anode and cathode overpotentials (η_a and η_c) are determined from the half-cell SOR or CO$_2$RR test, which are estimated as ~0.24 and ~0.48 V at 100 mA/cm^2, respectively. The voltage loss (E_m) at the membrane was estimated as ~0.24 V based on the resistance of the Nafion membrane in 3 M KOH. Further subtracting the membrane resistance from the full cell resistance measured under 100 mA/cm^2 operation, the voltage loss (E_S) caused by solution resistance and electrolyte polarization was obtained, which was ~0.53 V. Taking the potential difference of the asymmetric electrolyte into consideration, there still existed a voltage loss of ~0.33 V, which can be assigned to the errors in resistance determination and other unconsidered voltage-consuming factors (such as wire-connecting resistance, Nernstian pH losses) [54]. We can conclude that the η_c and E_s consume most of the energy input. The strategies of adopting a more efficient cathode material and using a slimmer flow chamber are thought to be effective to reduce the electricity demand of our CO$_2$RR-SOR electrolyzer.

Based on the performance of our electrolyzer, we also conducted a preliminary economic evaluation of the CO$_2$RR-SOR electrolysis process (Fig. 4f). The gross profit margin of the electrolyzer per unit electric input was calculated based on the cell voltage, the FE of the CO$_2$ reduction products and the revenues of the cathode and anode products. The capital investments and operation costs were converted into the electricity input cost, where the converting factors for equivalent electricity price (0.03 $/kWh) were set as 9 times considering the costs of electrolyzers, chemicals and operation maintenance, product

separation, etc. As HCOO⁻ was produced as the main cathode product, the gross cell revenue per unit electricity input of our CO_2RR-SOR electrolysis system was estimated as 0.35 $/kWh, which is much higher than that of the CO_2RR-OER process (0.18 $/kWh) (Fig. 4f). The net revenue of the former (0.32 $/kWh) is then more than 2 times that of the latter (0.15 $/kWh). The gross revenue of the current CO_2RR-SOR electrolyzer can cover the total cost equivalent to more than 11.6 times the electricity price. If the total input cost becomes higher, it is necessary to reduce the cell voltage to make a positive net profit. When operating the CO_2RR-SOR at a full cell voltage of 1.8 V or 1.0 V, the CO_2RR-SOR electrolyzer could achieve a gross revenue output of 0.43 $/kWh or 0.77 $/kWh, respectively, indicating the effectiveness of decreasing the operation voltage to increase the economic revenue. If we further consider the cost decrease by the usage of green electricity and the additional eco-benefits of CO_2 mitigation and sulfide removal, the CO_2RR-SOR co-electrolysis process may possess a higher revenue output.

At last, we demonstrated a solar-driven PV-EC system by powering the CO_2RR-SOR electrolyzer with a commercial Si PV cell (Figs. 5a and S20). Under the irradiation of 100 mW/cm², a theoretical current density of ~125 mA/cm² was expected for the PV-EC system (Fig. S21). Initially, the self-powered PV-EC device for CO_2RR-SOR yielded a current density output of ~120 mA/cm². While, with the test continued, the performance of the device decayed with the current density slowly decreasing to 100 mA/cm² in 6 h (Fig. 5b). During the 6 h of operation, the HCOO⁻ was continuously produced at the cathode with the FE

maintaining at ~95% (Figs. 5b and S22a). The concentration of S_2^{2-} at the anode also kept increasing with a yielding rate of 10.6 mM/h, corresponding to an S^{2-} degradation rate of 4.12 mmol/h (Figs. 5b and S22b). When we counted the energy that stored in the cathode products, the solar-to-carbon (STC) efficiency of this self-biased PV-EC system was estimated as $5.8 \pm 0.4\%$. As the operating current density of this PV-EC system is actually restricted by the short-circuit current density of the solar cell module, the STC efficiency of our device should be even higher if a matched high-efficient solar cell was applied. Nevertheless, few PV-EC devices that use Si PV cells have been reported for solar-driven CO_2RR under such high current density and long operating duration (Fig. 5c, Table S6) [55–62].

To further elucidate the energy-saving characteristic of the CO_2RR-SOR couple, we also performed the CO_2RR-SOR co-electrolysis for C_{2+} chemical production, where an electro-reduced Cu cathode was adopted. We prepared the electro-reduced Cu GDE from the Cu(OH)F powder precursor. The structure and microscopy analysis show that the small copper particles with abundant edges were formed as the active catalysts (Fig. S23). When the ER-Cu GDE||S-Cu:Co@NF cell was constructed, the CO_2RR-SOR electrolysis showed a low onset cell potential of 0.5 V and delivered a current density of 100 mA/cm² at 1.80 V, saving 42% of the electricity demand relative to the CO_2RR-OER one (Fig. S24a). During the polarization, the H_2, C_1 (CO, HCOO⁻) and C_{2+} (C_2H_4, C_2H_5OH, n-C_3H_7OH and CH_3COO^-) chemicals were produced, where CO is the major C_1 product and C_2H_4, C_2H_5OH are the major C_{2+} products (Fig. S24b). The ER-Cu GDE||S-Cu:Co@NF also showed a good stability
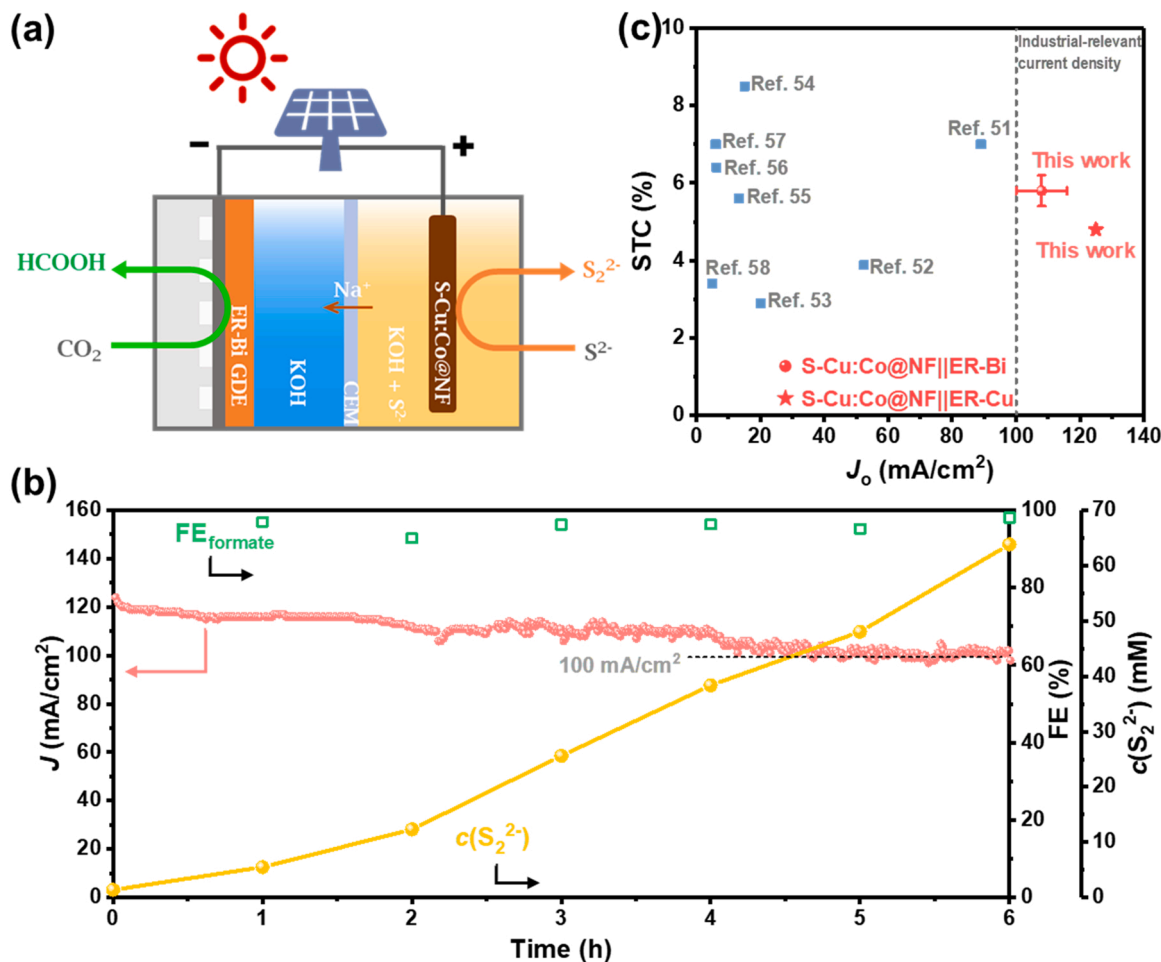
Fig. 5. (a) Schematic of a solar-driven PV-EC system coupling CO_2RR and SOR. (b) 6 h of operation of the solar-driven CO_2RR-SOR device showing the current density-time curve, the Faradaic efficiencies of HCOO⁻ product, and the accumulation of the S_2^{2-} species during the test. (c) Comparison of the performance of solar-driven CO_2RR devices adopting Si-based PV cells.

to be operated at 100 mA/cm^2 for 24 h (Fig. S24c). The economic analysis based on the production of C$_2$H$_4$ also suggests that the gross cell revenue per unit electricity input for CO$_2$RR-SOR (0.093 \$/kWh) was much higher than that of CO$_2$RR-OER (0.019 \$/kWh) (Fig. S25). It should be noted that the economic return of CO$_2$RR-SOR couple for C$_2$H$_4$ production is less than that for HCOO$^-$ production, which could be attributed to the lower FE and the smaller profit per electric quantity of C$_2$H$_4$ as compared to HCOO$^-$ product. When powered with the Si PV cell, a stable current density of ~125 mA/cm^2 and a C$_{2+}$ FE of ~49.8% were obtained, where the STC efficiency was calculated as 4.8% (Figs. 5c and S26).

4. Conclusion

In summary, we demonstrated an energy-saving co-valorization process by coupling CO$_2$RR with SOR. The value-added CO$_2$-reduction chemicals and sulfur solids were produced from the greenhouse CO$_2$ gas and toxic sulfide wastes with a reduced electricity input, advancing the economic profitability and environmental sustainability. At the anode, benefiting from the accelerated kinetics for SOR, the S, Cu-dual doped cobalt hydroxides could oxidize the aqueous sulfide to launch a current density of 100 mA/cm^2 at a rather low potential of 0.381 V vs RHE. At the cathode, the gas diffusion electrode with electrochemical-reduced Bi catalyst achieved CO$_2$ reduction at the same current density with a cathode potential of $-$0.648 V vs RHE. When working together, the hybrid electrolyzer assembled from the two electrodes enables the operation of CO$_2$RR-SOR co-electrolysis at 100 mA/cm^2 with a low full-cell voltage of ~2.1 V, cutting 40% of the energy request with respect to the CO$_2$RR-OER counterpart. Voltage breakdown analysis and technoeconomic evaluation of the two-electrode CO$_2$RR-SOR electrolyzer indicated that reducing the cell resistance as well as the catalyst overpotential for CO$_2$ reduction are promising to improve the economic feasibility of the system for practical applications. The self-powered CO$_2$RR-SOR co-electrolysis was also demonstrated by integrating the hybrid electrolyzer into a commercial photovoltaic cell. Under 1 Sun irradiation, the PV-EC device for CO$_2$RR-SOR stably operated at a current density of more than 100 mA/cm^2 for 6 h, where a solar-conversion efficiency of 5.8 $\pm$ 0.4% was achieved. Further replacing the cathode with an ER-Cu catalyst, a low cell voltage of 1.8 V was achieved for operating at 100 mA/cm^2, where C$_{2+}$ chemicals were produced as the main product. Similarly, powered by the Si PV cell, a stable current density of 125 mA/cm^2 and an STC efficiency of 4.8% were obtained. Our work offers a promising co-valorization strategy for carbon-neutral utilization and waste treatment with better sustainability.

CRediT authorship contribution statement

Kaixin Yang: Investigation, Data curation, Writing – original draft. **Nan Zhang:** Data curation, Formal analysis. **Jiangfan Yang:** Investigation, Validation. **Zhuo Xu:** Data curation. **Junqing Yan:** Writing – review & editing, Resources. **Deng Li:** Conceptualization, Data curation, Writing – original draft, Visualization. **Shengzhong (Frank) Liu:** Writing – review & editing, Resources, Supervision, Funding acquisition.

Declaration of Competing Interest

The authors declare that they have no known competing financial interests or personal relationships that could have appeared to influence the work reported in this paper.

Data availability

The data that has been used is confidential.

Appendix A. Supplementary material

Supplementary data associated with this article can be found in the online version at doi:10.1016/j.apcatb.2023.122718.

References

[1] Z. Liu, Z. Deng, G. He, H. Wang, X. Zhang, J. Lin, Y. Qi, X. Liang, Challenges and opportunities for carbon neutrality in China, Nat. Rev. Earth Environ. 3 (2022) 141–155, https://doi.org/10.1038/s43017-021-00244-x.

[2] D. Li, K. Yang, J. Lian, J. Yan, S. Liu, Powering the world with solar fuels from photoelectrochemical CO$_2$ reduction: basic principles and recent advances, Adv. Energy Mater. 12 (2022), 2201070, https://doi.org/10.1002/aenm.202201070.

[3] P.D. Luna, C. Hahn, D. Higgins, S.A. Jaffer, T.F. Jaramillo, E.H. Sargent, What would it take for renewably powered electrosynthesis to displace petrochemical processes? Science 364 (2019) eaav3506, https://doi.org/10.1126/science.aav3506.

[4] G. Wang, J. Chen, Y. Ding, P. Cai, L. Yi, Y. Li, C. Tu, Y. Hou, Z. Wen, L. Dai, Electrocatalysis for CO$_2$ conversion: from fundamentals to value-added products, Chem. Soc. Rev. 50 (2021) 4993–5061, https://doi.org/10.1039/D0CS00071J.

[5] S. Verma, B. Kim, H.-R.M. Jhong, S. Ma, P.J.A. Kenis, A gross-margin model for defining technoeconomic benchmarks in the electroreduction of CO$_2$, ChemSusChem 9 (2016) 1972–1979, https://doi.org/10.1002/cssc.201600394.

[6] M. Jouny, W. Luc, F. Jiao, General techno-economic analysis of CO$_2$ electrolysis systems, Ind. Eng. Chem. Res. 57 (2018) 2165–2177, https://doi.org/10.1021/acs.iecr.7b03514.

[7] S. Verma, S. Lu, P.J.A. Kenis, Co-electrolysis of CO$_2$ and glycerol as a pathway to carbon chemicals with improved technoeconomics due to low electricity consumption, Nat. Energy 4 (2019) 466–474, https://doi.org/10.1038/s41560-019-0374-6.

[8] H. Shin, K.U. Hansen, F. Jiao, Techno-economic assessment of low-temperature carbon dioxide electrolysis, Nat. Sustain. 4 (2021) 911–919, https://doi.org/10.1038/s41893-021-00739-x.

[9] Á. Vass, B. Endrődi, C. Janáky, Coupling electrochemical carbon dioxide conversion with value-added anode processes: an emerging paradigm, Curr. Opin. Electrochem. 25 (2021), 100621, https://doi.org/10.1016/j.coelec.2020.08.003.

[10] J. Na, B. Seo, J. Kim, C.W. Lee, H. Lee, Y.J. Hwang, B.K. Min, D.K. Lee, H.-S. Oh, U. Lee, General technoeconomic analysis for electrochemical coproduction coupling carbon dioxide reduction with organic oxidation, Nat. Commun. 10 (2019) 5193, https://doi.org/10.1038/s41467-019-12744-y.

[11] L. Chen, J. Shi, Co-electrolysis toward value-added chemicals, Sci. China Mater. 65 (2022) 1–9, https://doi.org/10.1007/s40843-011-1809-5.

[12] Z. Xu, C. Peng, G. Zheng, Coupling value-added anodic reactions with electrocatalytic CO$_2$ reduction, Chem. Eur. J. 29 (2023), e202203147, https://doi.org/10.1002/chem.202203147.

[13] X. Wei, Y. Li, L. Chen, J. Shi, Formic acid electro-synthesis by concurrent cathodic CO$_2$ reduction and anodic CH$_3$OH oxidation, Angew. Chem. Int. Ed. 60 (2021) 3148–3155, https://doi.org/10.1002/anie.202012066.

[14] J.-Y. Song, C. Kim, M. Kim, K.M. Cho, I. Gereige, W.-B. Jung, H. Jeong, H.-T. Jung, Generation of high-density nanoparticles in the carbothermal shock method, Sci. Adv. 7 (2021) eabk2984, https://doi.org/10.1126/sciadv.abk2984.

[15] K. Petrov, S. Srinivasan, Low temperature removal of hydrogen sulfide from sour gas and its utilization for hydrogen and sulfur production, Int. J. Hydrog. Energy 21 (1996) 163–169, https://doi.org/10.1016/0360-3199(95)00003-8.

[16] L. Zhang, Z. Wang, J. Qiu, Energy-saving hydrogen production by seawater electrolysis coupling sulfion degradation, Adv. Mater. 34 (2022), 2109321, https://doi.org/10.1002/adma.202109321.

[17] E. Vaiopoulou, T. Provijn, A. Prévoteau, I. Pikaar, K. Rabaey, Electrochemical sulfide removal and caustic recovery from spent caustic streams, Water Res. 92 (2016) 38–43, https://doi.org/10.1016/j.watres.2016.01.039.

[18] T. Burdyny, W.A. Smith, CO$_2$ reduction on gas-diffusion electrodes and why catalytic performance must be assessed at commercially-relevant conditions, Energy Environ. Sci. 12 (2019) 1442–1453, https://doi.org/10.1039/C8EE03134G.

[19] B.M. Tackett, E. Gomez, J.G. Chen, Net reduction of CO$_2$ via its thermocatalytic and electrocatalytic transformation reactions in standard and hybrid processes, Nat. Catal. 2 (2019) 381–386, https://doi.org/10.1038/s41929-019-0266-y.

[20] W. Ma, H. Wang, W. Yu, X. Wang, Z. Xu, X. Zong, C. Li, Achieving simultaneous CO$_2$ and H$_2$S conversion via a coupled solar-driven electrochemical approach on non-precious-metal catalysts, Angew. Chem. Int. Ed. 57 (2018) 3473–3477, https://doi.org/10.1002/anie.201713029.

[21] T. Luo, J. Bai, J. Li, Q. Zeng, Y. Ji, L. Qiao, X. Li, B. Zhou, Self-driven photoelectrochemical splitting of H$_2$S for S and H$_2$ recovery and simultaneous electricity generation, Environ. Sci. Technol. 51 (2017) 12965–12971, https://doi.org/10.1021/acs.est.7b03116.

[22] B. Zhang, J. Bai, Y. Zhang, C. Zhou, P. Wang, L. Zha, J. Li, A. Simchi, B. Zhou, High yield of CO and synchronous S recovery from the conversion of CO_2 and H_2S in natural gas based on a novel electrochemical reactor, Environ. Sci. Technol. 55 (2021) 14854–14862, https://doi.org/10.1021/acs.est.1c04414.

[23] C. Xiao, L. Cheng, Y. Wang, J. Liu, R. Chen, H. Jiang, Y. Li, C. Li, Low full-cell voltage driven high-current-density selective paired formate electrosynthesis, J. Mater. Chem. A 10 (2022) 1329–1335, https://doi.org/10.1039/D1TA08303A.

[24] C. Xia, P. Zhu, Q. Jiang, Y. Pan, W. Liang, E. Stavitski, H.N. Alshareef, H. Wang, Continuous production of pure liquid fuel solutions via electrocatalytic CO_2 reduction using solid-electrolyte devices, Nat. Energy 4 (2019) 776–785, https://doi.org/10.1038/s41560-019-0451-x.

[25] G. Kresse, J. Furthmüller, Efficient iterative schemes for AB initio total-energy calculations using a plane-wave basis set, Phys. Rev. B 54 (1996) 11169–11186, https://doi.org/10.1103/PhysRevB.54.11169.

[26] G. Kresse, J. Furthmüller, Efficiency of AB-initio total energy calculations for metals and semiconductors using a plane-wave basis set, Comput. Mater. Sci. 6 (1996) 15–50, https://doi.org/10.1016/0927-0256(96)00008-0.

[27] J.P. Perdew, K. Burke, M. Ernzerhof, Generalized gradient approximation made simple, Phys. Rev. Lett. 77 (1996) 3865–3868, https://doi.org/10.1103/PhysRevLett.77.3865.

[28] S. Grimme, Semiempirical GGA-type density functional constructed with a long-range dispersion correction, J. Comput. Chem. 27 (2006) 1787–1799, https://doi.org/10.1002/jcc.20495.

[29] J.A. Koza, C.M. Hull, Y.-C. Liu, J.A. Switzer, Deposition of β-$Co(OH)_2$ films by electrochemical reduction of tris(ethylenediamine)cobalt(III) in alkaline solution, Chem. Mater. 25 (2013) 1922–1926, https://doi.org/10.1021/cm400579k.

[30] Y.-C. Liu, J.A. Koza, J.A. Switzer, Conversion of electrodeposited $Co(OH)_2$ to CoOOH and Co_3O_4, and comparison of their catalytic activity for the oxygen evolution reaction, Electrochim. Acta 140 (2014) 359–365, https://doi.org/10.1016/j.electacta.2014.04.036.

[31] P. Gao, Y. Zeng, P. Tang, Z. Wang, J. Yang, A. Hu, J. Liu, Understanding the synergistic effects and structural evolution of $Co(OH)2$ and $Co3O4$ toward boosting electrochemical charge storage, Adv. Funct. Mater. 32 (2022), 2108644, https://doi.org/10.1002/adfm.202108644.

[32] S. Liu, R.-T. Gao, M. Sun, Y. Wang, T. Nakajima, X. Liu, W. Zhang, L. Wang, In situ construction of hybrid $Co(OH)_2$ nanowires for promoting long-term water splitting, Appl. Catal. B 292 (2021), 120063, https://doi.org/10.1016/j.apcatb.2021.120063.

[33] L. Aguilera, P.C.M. Aguiar, Y.L. Ruiz, A. Almeida, J.A. Moreira, R.R. Passos, L. A. Pocrifka, Electrochemical synthesis of γ-CoOOH films from α-$Co(OH)_2$ with a high electrochemical performance for energy storage device applications, J. Mater. Sci. Mater. Electron. 31 (2020) 3084–3091, https://doi.org/10.1007/s10854-019-02853-1.

[34] L. Chen, H. Zhang, L. Chen, X. Wei, J. Shi, M. He, Facile synthesis of Cu doped cobalt hydroxide (Cu–$Co(OH)_2$) nano-sheets for efficient electrocatalytic oxygen evolution, J. Mater. Chem. A 5 (2017) 22568–22575, https://doi.org/10.1039/C7TA07637A.

[35] H. Bian, T. Liu, D. Li, Z. Xu, J. Lian, M. Chen, J. Yan, S. Frank Liu, Unveiling the effect of interstitial dopants on CO_2 activation over $CsPbBr_3$ catalyst for efficient photothermal CO_2 reduction, Chem. Eng. J. 435 (2022) 135071, https://doi.org/10.1016/j.cej.2022.135071.

[36] T. Liu, X. Hong, G. Liu, In situ generation of the Cu@3D-ZrO_x framework catalyst for selective methanol synthesis from CO_2/H_2, ACS Catal. 10 (2020) 93–102, https://doi.org/10.1021/acscatal.9b03738.

[37] J. Yang, V. Smulders, J.J.T. Smits, B.T. Mei, G. Mul, Electrochemical oxidation of H_2S on polycrystalline Ni electrodes, J. Appl. Electrochem. 49 (2019) 929–936, https://doi.org/10.1007/s10800-019-01334-x.

[38] Y. Wu, Y. Zhao, P. Zhai, C. Wang, J. Gao, L. Sun, J. Hou, Triggering lattice oxygen activation of single-atomic Mo sites anchored on Ni–Fe oxyhydroxides nanoarrays for electrochemical water oxidation, Adv. Mater. 34 (2022), 2202523, https://doi.org/10.1002/adma.202202523.

[39] N. Zhang, C. Wang, J. Chen, C. Hu, J. Ma, X. Deng, B. Qiu, L. Cai, Y. Xiong, Y. Chai, Metal substitution steering electron correlations in pyrochlore ruthenates for efficient acidic water oxidation, ACS Nano 15 (2021) 8537–8548, https://doi.org/10.1021/acsnano.1c00266.

[40] M. Zhang, J. Guan, Y. Tu, S. Chen, Y. Wang, S. Wang, L. Yu, C. Ma, D. Deng, X. Bao, Highly efficient H_2 production from H_2S via a robust graphene-encapsulated metal catalyst, Energy Environ. Sci. 13 (2020) 119–126, https://doi.org/10.1039/C9EE03231B.

[41] A.A. Anani, Z. Mao, R.E. White, S. Srinivasan, A.J. Appleby, Electrochemical production of hydrogen and sulfur by low-temperature decomposition of hydrogen sulfide in an aqueous alkaline solution, J. Electrochem. Soc. 137 (1990) 2703–2709, https://doi.org/10.1149/1.2087021.

[42] Z.W. Seh, J. Kibsgaard, C.F. Dickens, I. Chorkendorff, J.K. Nørskov, T.F. Jaramillo, Combining theory and experiment in electrocatalysis: Insights into materials design, Science 355 (2017) eaad4998, https://doi.org/10.1126/science.aad4998.

[43] T. Wang, P. Wang, W. Zang, X. Li, D. Chen, Z. Kou, S. Mu, J. Wang, Nanoframes of Co_3O_4–Mo_2N heterointerfaces enable high-performance bifunctionality toward both electrocatalytic HER and OER, Adv. Funct. Mater. (2021), 2107382, https://doi.org/10.1002/adfm.202107382. N./a.

[44] W. Yu, J. Yu, Y. Wang, X. Li, Y. Wang, H. Yuan, X. Zhang, H. Liu, W. Zhou, Electrocatalytic upcycling of nitrate and hydrogen sulfide via a nitrogen-doped carbon nanotubes encapsulated iron carbide electrode, Appl. Catal. B 310 (2022), 121291, https://doi.org/10.1016/j.apcatb.2022.121291.

[45] S. Zhang, Q. Zhou, Z. Shen, X. Jin, Y. Zhang, M. Shi, J. Zhou, J. Liu, Z. Lu, Y.-N. Zhou, H. Zhang, Sulfophobic and vacancy design enables self-cleaning electrodes for efficient desulfurization and concurrent hydrogen evolution with low energy consumption, Adv. Funct. Mater. 31 (2021), 2101922, https://doi.org/10.1002/adfm.202101922.

[46] Y. Li, Y. Duan, K. Zhang, W. Yu, Efficient anodic chemical conversion to boost hydrogen evolution with low energy consumption over cobalt-doped nickel sulfide electrocatalyst, Chem. Eng. J. 433 (2022), 134472, https://doi.org/10.1016/j.cej.2021.134472.

[47] Y. Pei, J. Cheng, H. Zhong, Z. Pi, Y. Zhao, F. Jin, Sulfide-oxidation-assisted electrochemical water splitting for H_2 production on a bifunctional Cu_2S/nickel foam catalyst, Green Chem. 23 (2021) 6975–6983, https://doi.org/10.1039/D1GC01857D.

[48] M. Kumar, T.C. Nagaiah, Efficient production of hydrogen from H_2S via electrolysis using a $CoFeS_2$ catalyst, J. Mater. Chem. A 10 (2022) 7048–7057, https://doi.org/10.1039/D1TA09888H.

[49] M. Kumar, T.C. Nagaiah, Pure hydrogen and sulfur production from H_2S by an electrochemical approach using a NiCu–MoS_2 catalyst, J. Mater. Chem. A 10 (2022) 13031–13041, https://doi.org/10.1039/D2TA02751H.

[50] G. Wang, J. Chen, K. Li, J. Huang, Y. Huang, Y. Liu, X. Hu, B. Zhao, L. Yi, T. W. Jones, Z. Wen, Cost-effective and durable electrocatalysts for co-electrolysis of CO_2 conversion and glycerol upgrading, Nano Energy 92 (2022), 106751, https://doi.org/10.1016/j.nanoen.2021.106751.

[51] D. Wu, J. Hao, Z. Song, X. Fu, J. Luo, All roads lead to rome: an energy-saving integrated electrocatalytic CO_2 reduction system for concurrent value-added formate production, Chem. Eng. J. 412 (2021), 127893, https://doi.org/10.1016/j.cej.2020.127893.

[52] Y. Li, C. Huo, H. Wang, Z. Ye, P. Luo, X. Cao, T. Lu, Coupling CO_2 reduction with CH_3OH oxidation for efficient electrosynthesis of formate on hierarchical bifunctional CuSn alloy, Nano Energy 98 (2022), 107277, https://doi.org/10.1016/j.nanoen.2022.107277.

[53] X.V. Medvedeva, J.J. Medvedev, S.W. Tatarchuk, R.M. Choueiri, A. Klinkova, Sustainable at both ends: electrochemical CO_2 utilization paired with electrochemical treatment of nitrogenous waste, Green Chem. 22 (2020) 4456–4462, https://doi.org/10.1039/D0GC01754J.

[54] C.M. Gabardo, C.P. O'Brien, J.P. Edwards, C. McCallum, Y. Xu, C.-T. Dinh, J. Li, E. H. Sargent, D. Sinton, Continuous carbon dioxide electroreduction to concentrated multi-carbon products using a membrane electrode assembly, Joule 3 (2019) 2777–2791, https://doi.org/10.1016/j.joule.2019.07.021.

[55] S.Y. Chae, S.Y. Lee, S.G. Han, H. Kim, J. Ko, S. Park, O.-S. Joo, D. Kim, Y. Kang, U. Lee, Y.J. Hwang, B.K. Min, A perspective on practical solar to carbon monoxide production devices with economic evaluation, Sustain. Energy Fuels 4 (2020) 199–212, https://doi.org/10.1039/C9SE00647H.

[56] Z. Chen, T. Wang, B. Liu, D. Cheng, C. Hu, G. Zhang, W. Zhu, H. Wang, Z.-J. Zhao, J. Gong, Grain-boundary-rich copper for efficient solar-driven electrochemical CO_2 reduction to ethylene and ethanol, J. Am. Chem. Soc. 142 (2020) 6878–6883, https://doi.org/10.1021/jacs.0c00971.

[57] G.M. Sriramagiri, N. Ahmed, W. Luc, K.D. Dobson, S.S. Hegedus, F. Jiao, Toward a practical solar-driven CO_2 flow cell electrolyzer: design and optimization, ACS Sustain. Chem. Eng. 5 (2017) 10959–10966, https://doi.org/10.1021/acssuschemeng.7b02853.

[58] G. Piao, S.H. Yoon, D.S. Han, H. Park, Ion-enhanced conversion of CO_2 into formate on porous dendritic bismuth electrodes with high efficiency and durability, ChemSusChem 13 (2020) 698–706, https://doi.org/10.1002/cssc.201902581.

[59] J. Gurudayal, D.F. Bullock, C.M. Srankó, Y. Towle, M. Lum, M.C. Hettick, A. Scott, J. Javey Ager, Efficient solar-driven electrochemical CO_2 reduction to hydrocarbons and oxygenates, Energy Environ. Sci. 10 (2017) 2222–2230, https://doi.org/10.1039/C7EE01764B.

[60] D. Ren, N.W.X. Loo, L. Gong, B.S. Yeo, Continuous production of ethylene from carbon dioxide and water using intermittent sunlight, ACS Sustain. Chem. Eng. 5 (2017) 9191–9199, https://doi.org/10.1021/acssuschemeng.7b02110.

[61] B.-j Kim, G. Piao, S. Kim, S.Y. Yang, Y. Park, D.S. Han, H.K. Shon, M.R. Hoffmann, H. Park, High-efficiency solar desalination accompanying electrocatalytic conversions of desalted chloride and captured carbon dioxide, ACS Sustain. Chem. Eng. 7 (2019) 15320–15328, https://doi.org/10.1021/acssuschemeng.9b02640.

[62] T. Arai, S. Sato, K. Sekizawa, T.M. Suzuki, T. Morikawa, Solar-driven CO_2 to CO reduction utilizing H_2O as an electron donor by earth-abundant Mn–bipyridine complex and Ni-modified Fe-oxyhydroxide catalysts activated in a single-compartment reactor, Chem. Commun. 55 (2019) 237–240, https://doi.org/10.1039/C8CC07900E.